Towards an application of muon scattering tomography as a technique for detecting rebars in concrete

OPEN ACCESS
IOP Publishing
Smart Materials and Structures
Smart Mater. Struct. **29** (2020) 055015 (15pp)
https://doi.org/10.1088/1361-665X/ab7a3f

Towards an application of muon scattering tomography as a technique for detecting rebars in concrete

Magdalena Dobrowolska[1], Jaap Velthuis[1,2], Anna Kopp[1], Marcus Perry[3] and Philip Pearson[4]

[1] School of Physics, HH Wills Physics Laboratory, University of Bristol, Tyndall Avenue, BS8 1TL, Bristol, United Kingdom
[2] School of Nuclear Science and Technology, University of South China, No 28 West Changsheng Rd, Hengyang, People's Republic of China
[3] Civil and Environmental Engineering, University of Strathclyde, James Weir Building, 75 Montrose Street, Glasgow, G1 1XJ, United Kingdom
[4] Cavendish Nuclear, Civil Structural & Architectural (CS&A) Department, Babcock Technology Centre (BTC), Unit 100A, Bristol Business Park, Stoke Gifford, BS16 1EJ, United Kingdom

E-mail: m.dobrowolska@bristol.ac.uk

Received 21 October 2019, revised 28 January 2020
Accepted for publication 26 February 2020
Published 31 March 2020

Abstract

Inspection of the world's ageing population of reinforced concrete infrastructure is a multi-billion dollar problem. Historically, it has not been uncommon for structures to deviate from their designs,or for design drawings to be lost. This leaves asset managers the challenging task of making structural health assessments and maintenance decisions with incomplete knowledge. While current techniques for detecting rebars in concrete are typically limited to penetration depths of less than 50 cm, muon scattering tomography (MST) is a non-destructive, non-invasive technique which shows great promise for high-depth 3D concrete imaging. This paper uses Monte Carlo simulations to demonstrate that MST can be used to detect and locate 100 cm length rebars with a diameter of 33.7 $\pm$ 7.3 mm independently of the rebar's location within a concrete structure. This corresponds to a volume of inclusion of 894 $\pm$ 386 cm^3. The volume of the inclusion can be reconstructed with a resolution of 5.4 $\pm$ 0.3% for volumes above 2 500 cm^3. It is furthermore demonstrated that 30 mm diameter rebars can be distinguished as two separate objects provided their separation is more than 40–60 mm, and that single and double layers of rebars are distinguishable using the technique. It is anticipated that MST could inform practical studies which support more informed maintenance and modeling, eventually allowing digital twins to be created for a larger subset of historical steel and concrete structures.

Keywords: 3D imaging, concrete imaging, reinforcement location, rebar location

(Some figures may appear in colour only in the online journal)

1. Introduction

Currently there are limited non-destructive evaluation (NDE) techniques in civil and structural engineering to ascertain the configuration of steelwork within reinforced concrete structures to a high depth. A particular problem, typically for construction over the period pre1900–2010, is that the original design philosophy and construction detailed

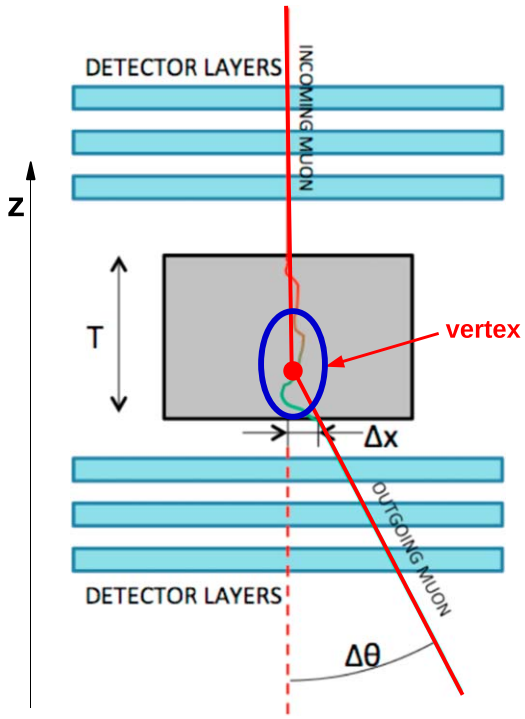

Figure 1. Muon scattering tomography principle [11].

reinforcement drawings may not have survived or are unreliable and not showing the 'as built'-condition. In the UK and in much of Europe, a post-war shortage of reinforcement has resulted in steel variations from both the design code and construction specification. Also the variable nature of workmanship and site supervision has presented the construction industry numerous challenges in the management of errors [1].

Current NDE scanning technology is limited to the detection of reflected or transmitted electromagnetic, thermal or acoustic waves generated by a local source. The return-time, magnitude, polarization or angle of waves after interaction with the structure can be used to reconstruct an image of the reinforcement configuration and the approximate corrosion state. Current commercial solutions (electromagnetic cover-meters) make use of safe, low-energy methods based on reflected radar, sonar or heat. A weakness that all these methods share is that the top layer of reinforcement (steel rebar) masks deeper features and this can make it impossible to image beyond 200 mm depths in congested areas.

Specialists NDE firms and researchers can opt for NDE techniques which involve the transmission of high energy particles through the structure, such as x-rays, gamma rays or neutrons [2–4]. Their longer penetration depths allow for high resolution tomography, but these methods are not routinely used as they pose a substantial radiation hazard to operators, assets and environments. In the energy generation sector, these techniques also pose a risk to electrical control systems.

Muon tomography exploits benign background radiation with no effect on instrumentation or to personnel. More discussion on different imaging techniques is in section 7.1. It is a very appropriate technique to image large scale structures like pyramids [5], volcanoes [6] or buildings like the Fukushima Daiichi reactor [7, 8], scan cargo container to detect large objects containing special nuclear materials [9, 10], image nuclear waste [11], discriminate high-Z materials in concrete-filled containers [12] and detect gases in concrete filled drums [13]. The size measurements for uranium blocks in concrete have been done [14] and yielded 2.9 ± 0.5 mm resolution on the edges. However the performance for steel will be worse and walls are thicker than the drums used in the study presented in [14]. In this paper we present a method to detect, locate and image rebars in concrete structures as well as to separate multiple rebars using a decision algorithm.

The approach to use muon scattering tomography (MST) for the detection high-density materials in concrete is based on the procedure described in [9] and is further developed here for the application of scanning concrete objects in search of rebars (modeled as iron rods). In this work, we use Monte Carlo simulations of a MST system.

2. Muon scattering tomography

2.1. Overview

Cosmic rays are high energy, charged particles which arrive at the Earth's atmosphere from outer space. When primary cosmic rays interact with nuclei in the upper atmosphere, a cascade of the secondary cosmic rays is produced. Large part of secondary particles are pions which swiftly decay producing muons. Muons are identical to electrons, except that they are 200 times heavier. They are the main type of particles coming from cosmic ray interactions that reach at sea level. Due to its much higher mass, muons do not scatter very much and thus can traverse large amount of material.

MST is a method employed for the examination of material volumes from a safe distance. MST is based on the multiple Coulomb scattering of cosmic muons in matter. When a charged particle traverses matter, it interacts with the electric fields of the electron clouds and of the nuclei in the matter. This leads to a series of tiny, random changes in direction. As a result the charged particle exits the material at an angle with respect to the incoming direction. This is known as multiple scattering. The angle is not fixed but obeys a well known spectrum that depends on the material type, its thickness and the particle momentum. MST imaging relies on reconstructing the muon trajectories before and after leaving the scanned object, see figure 1 (set-up of the system is explained in section 2.3).

MST has been developed and applied for many different purposes [5–13, 15–20]. The primary advantage is that the scanning process is non-invasive and safe, both for people performing the scan and for the object being scanned. Cosmic muons are ubiquitous, so no additional source of artificial and harmful radiation is needed to examine the object. At sea level, the cosmic muon flux is about 10 000 m^{-2} min^{-1} [21]. It has a broad angular and momentum spread, see figure 2. As a consequence of this, the imaging can be done using

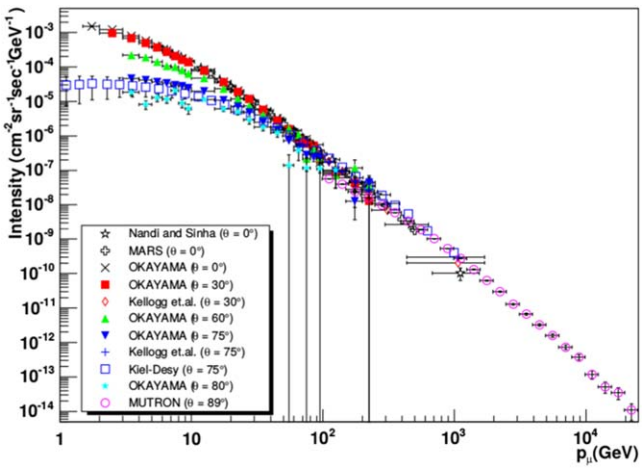

Figure 2. Muon intensity versus muon momentum, where θ is the zenith angle [22].

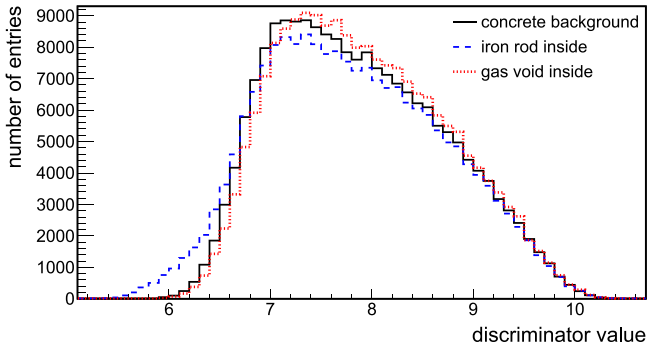

Figure 3. The discriminator distribution for the concrete-filled object (solid, black line), concrete-filled object with rebar inside (dashed, blue line) and concrete-filled object with gas void inside (dotted, red line).

sandwiched detector stacks above or below, or at angles to the structure. Since cosmic muons are deeply penetrating, do not interact strongly with matter, they can be used for imaging vast and dense volumes. Additionally, muons are also excellent probes when the examined object is encased by metal or rock [20]. Muons are charged particles, so it is relatively easy to detect them.

The angular distribution of scattering of muons can be characterized by a Gaussian distribution with a mean of zero and a standard deviation σ_θ, which depends on the atomic number, Z, of the traversed material. The standard deviation is described by [23]:

$$\sigma_\theta \approx \frac{13.6\ \text{MeV}}{pc\beta}\sqrt{\frac{T}{X_0}}\left[1 + 0.038\ln\left(\frac{T}{X_0}\right)\right], \quad (1)$$

$$X_0 \approx \frac{716.4A}{Z(Z+1)\ln\left(\frac{287}{\sqrt{Z}}\right)}\ (\text{g cm}^{-2}), \quad (2)$$

where p is muon's momentum, β its speed divided by the speed of light c, T is the thickness of the material and X_0 the radiation length of the traversed material and A is the atomic weight of the medium in g mol^{-1}.

2.2. Muon imaging

Several MST imaging methods exist. They all differ in the way they exploit the information of the incoming and outgoing tracks [24–26]. In our approach it is assumed that the incoming and outgoing muon paths intersect at a common point named a vertex. Since muons undergo multiple scattering in matter, this vertex approximation is not entirely accurate. However, it was shown that it is a very useful assumption which gives roughly the correct scatter location and a scattering angle of a muon. This method was successfully used to detect objects with a high atomic number (high-Z objects) in cargo containers [9, 10], image of nuclear waste [11], discriminate high-Z materials in concrete-filled containers [12] and detect voids in concrete filled drums [13], including distinguishing between a big void of gas from two smaller gas voids. Here, the approach was further expanded and adopted to industrial applications for the detection of rebars in concrete.

The method used here is described in detail in [9][5]. The basis of this method is that the scanned volume is divided into voxels. The voxel sides in the present study are 10 mm long. The muon tracks are fitted under the assumption that the scattering occurs in a single location, the vertex, and the scattering angle is extracted. Based on the vertex location, the track is assigned to a voxel. For each voxel the weighted metric, $\widetilde{m_{ij}}$, is calculated for each pair of vertices for the N most scattered tracks, where:

$$\widetilde{m_{ij}} = \frac{\|\boldsymbol{V_i} - \boldsymbol{V_j}\|}{\theta_i \cdot \theta_j}, \quad (3)$$

where $\boldsymbol{V_i}$ is the location of the vertex of muon i, θ_i is the corresponding scattering angle. The median of the weighted metric distribution is calculated for every voxel. The median of this distribution is then used as a discriminator: a metric used for measurement and detection of the inclusion [9]. In low atomic number (low-Z) materials, high-angle scattering happens less frequently than in denser materials. Therefore, in less dense matter, vertices are located further apart and thus a higher discriminator value is found for lower-Z materials. An example of a discriminator distribution obtained for a solid concrete-filled object, a solid concrete-filled object with a rebar inserted and a solid concrete-filled object with a gas void is shown in figure 3. The distributions are clearly different and indeed the addition of the high-Z material (iron) leads to lower discriminator values and the addition of low-Z material (gas) results in higher discriminator values. A study of the detection of lower-Z materials (gas voids) in concrete-filled drums was already performed in [13].

2.3. Detector set-up

The schematic sketch of the set-up used in the simulations is shown in figure 4. The simulated detector geometry included

[5] However, for this study, the momentum information about the particles was not used because it is not possible to measure the momentum accurately enough to improve the analysis in a practical scenario for this application.

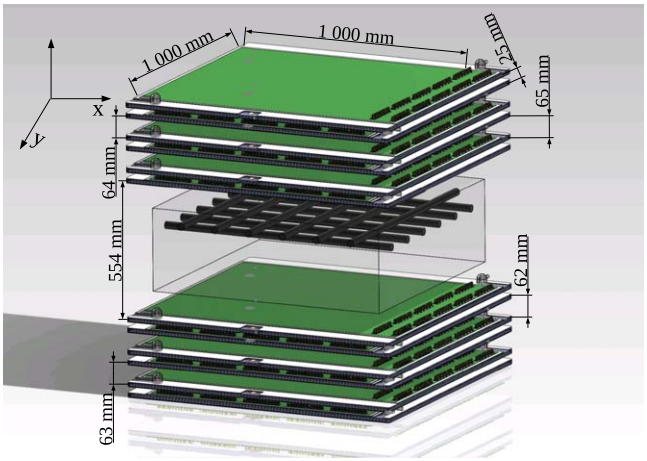

Figure 4. Schematic drawing of the set-up. Three double layers of RPCs are placed above and below the scanned object. Distances given in a image are center to center.

six pairs of resistive plate chambers (RPCs), shown in figure 5. Three of them are above and three below the scanned object. Three layers were chosen to ensure a precise reconstruction of the muon direction and thus the scattering angle. RPCs are detectors which have been used in high energy physics experiments for more than 30 years. RPCs consist of a gas volume over which a high voltage is applied. The muons, which are electrically charged, ionize the gas. Due to the high voltage a small spark is created locally. The spark induces signals which can be measured and the location where the muon entered the RPC can be reconstructed. They were chosen for this experiment because they are low cost, have a very good detector efficiency, sub-millimeter spatial resolution and large area detectors can be build [20]. One pair of RPCs houses both X and Y planes, perpendicular to each other, so they can measure both x and y coordinates of the muon paths to reconstruct them precisely. The scanned object is placed between the RPC stacks, as shown in figure 4. The RPCs' performance was modeled using the parameters of RPCs that were built for a container scanner prototype [20, 27] where RPCs had a pitch of 1.5 mm which resulted in a position resolution of approximately 450 μm. For the study presented here, the RPC planes were chosen to be $100 \times 100\,\mathrm{cm}^2$. The RPC is 6 mm thick. The distance between the X and Y planes was 19 mm and the distance between the pairs was 56–59 mm. The space, between top and bottom detector layers, for the object being scanned was 548 mm. Distances given here are edge to edge.

For the reconstructed tracks, variables related to the scattering behavior are calculated like the scattering angle, the χ^2 of the individual track fits for the incoming and outgoing muon tracks and the fit combining the incoming and outgoing muon tracks under the assumption that the scattering occurs in a single vertex.

2.4. Simulation details

The muons were generated using the CRY library [28], which is a reliable tool for generating realistic muon samples. The

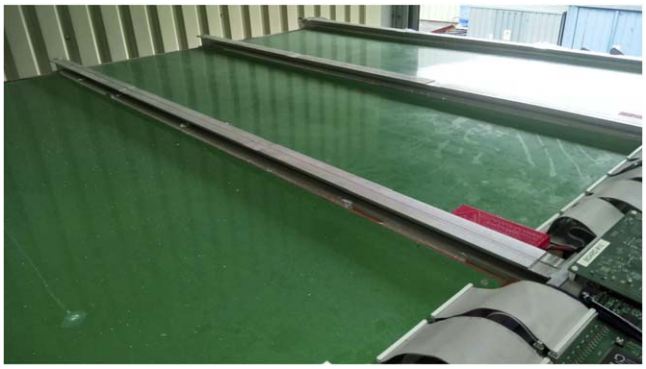

Figure 5. Resistive plate chambers.

traversing of the muons through the detectors and sample being scanning was simulated using GEANT4 [29]. GEANT4 is a toolkit created to perform Monte Carlo simulations of the passage of particles through matter and detectors. It is used in nuclear, high energy and accelerator physics as well in medical and space science. To perform a simulation, a geometry of the layout must be defined. The type of material that, the individual components of the system are made of, need to be specified as well. GEANT4 gives the possibility to choose the type of particles and physical processes that will be included in the simulation. The entire environment is based on the C ++ programming language.

Each time 216 million muons were simulated which corresponds to about three weeks of data taking at sea level. This time was selected as a compromise between acceptable measurement time for this particular application and the accuracy of the test. The voxel size was $10\,\mathrm{mm} \times 10\,\mathrm{mm} \times 10\,\mathrm{mm}$ and 30 muon vertices were required for a voxel to be considered in the analysis. Concrete was simulated as a material with a density of $2.3\,\mathrm{g\,cm}^{-3}$ and the rebars were simulated as iron bars with density of $7.87\,\mathrm{g\,cm}^{-3}$.

MST relies effectively on the differences in density between materials. The density of concrete varies between 2 and $2.5\,\mathrm{g\,cm}^{-3}$, while the density of steel is around $8\,\mathrm{g\,cm}^{-3}$. The results presented here will be very similar to studies using different concrete densities.

3. Simulation study scenarios

Three different scenarios were studied where rebars were represented by cylindrical iron rods. The rebar diameter was varied between 0 and 150 mm to study the sensitivity of the method and to see what the minimum detectable volume of rebar is. More details on the scenarios are given below. All the axes are analogous to the axes in figure 4.

3.1. Scenario 1: rebar inside variable size concrete block

The configuration of this scenario is shown in figure 6. In this scenario a rebar was placed in the center of a concrete cuboid. With the growing diameter of the rebar, the size of the cuboid was also increased so that there was always a 10 cm thick

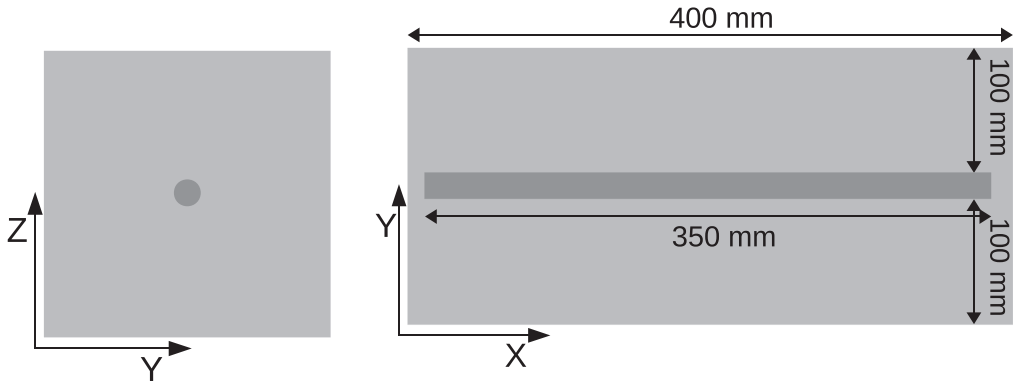

(a) Side (ZY) view (b) Top (YX) view

Figure 6. Dimensions of the scenario with the rebar inside a variable size concrete cuboid. The front (*ZX*) projection is identical to the top (*YX*) projection.

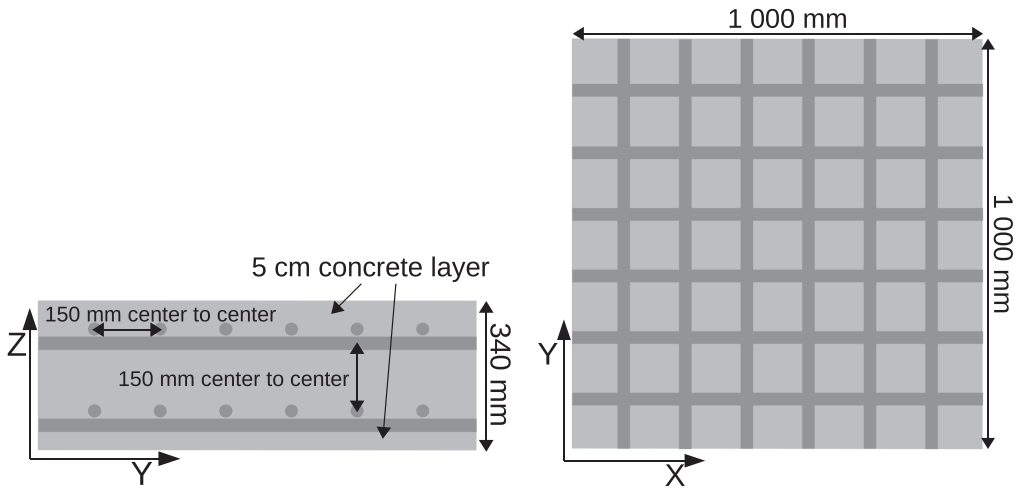

(a) Side (ZY) view (b) Top (YX) view

Figure 7. Reinforcement in fixed size concrete block: two double layers of rebars.

concrete cover. The smallest simulated concrete sample (without any rebar inside) was 20 cm × 20 cm × 40 cm. The concrete cuboid was always 40 cm long and the rebar always 35 cm long. For each different rebar diameter scenario a matching concrete background sample of the same dimensions was simulated.

3.2. Scenario 2: rebar inside fixed size concrete block

In this scenario, the size of the concrete cuboid was fixed at 100 cm × 100 cm × 50 cm. A 50 cm long rebar was placed in the center of the cuboid, but in contrast to scenario 1, the outer dimension of the concrete cuboid remained the same.

3.3. Scenario 3: reinforcement in concrete

The third scenario was designed to study the detection performance for reinforcement in concrete. The concrete block was sized 100 cm × 100 cm × 34 cm. This scenario was split into 4 different cases. First, a solid concrete block was generated as a background sample. Next, a single layer of rebars was introduced such that a layer of 5 cm of concrete was on top of the bars. The rebars had a diameter of 30 mm, were 100 cm long and the distance between them was 15 cm from center to center. Next, a second layer of the same rebars was placed directly underneath the top layer, perpendicular to the original direction. Finally, two double layers of rebars were introduced in the concrete and the distance between them was 15 cm from center to center. This case is illustrated in figure 7.

4. Signal extraction

For each of the scenarios, simulations were carried out. The analysis, summarized in section 2.2 and discussed in detail in [9], was performed to obtain discriminator distributions as shown in figure 3.

4.1. Signal definition

For this application, the signal extraction was modified from the one used in our previous work in [13]. A signal value (S) was calculated to indicate whether reinforcement is present in

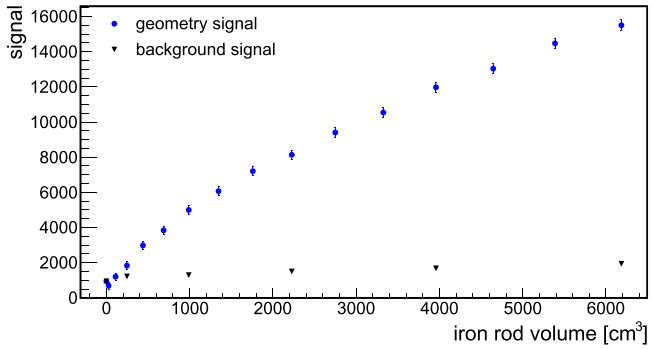

Figure 8. Signal as a function of the rebar volume for a variable size concrete block. Please note, that for this scenario, the volume of the concrete block, and thus also the background signal, grows. Black triangles show the signal value for a background cases, where the background samples have the same dimensions as geometries with rebars inside.

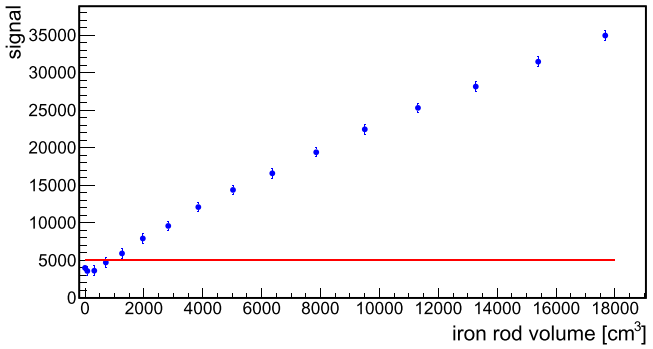

Figure 9. Signal as a function of the rebar volume for a fixed size concrete block. The signal (dots) shows a monotonic dependence on the rebar volume.

concrete and to determine its volume. Here, the signal is calculated as the sum of the absolute differences between bins in the discriminator distribution for a sample under investigation with a rebar (H_{rebar}) and a sample of concrete only (H_{concrete}), where the samples have the same dimensions

$$S = \sum_{bin} |H_{\text{rebar}}(i) - H_{\text{concrete}}(i)|. \quad (4)$$

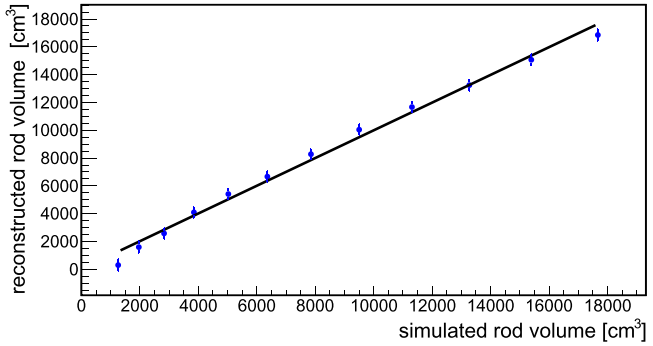

Figure 10. Reconstructed rebar volume as a function of simulated rebar volume.

5. Results: detection and sizing

5.1. Detection of rebars in concrete

Figure 8 shows the signal as a function of the rebar volume for the variable size concrete block scenario. The blue points refer to the signal calculated for the concrete with iron inclusions inside. The black points are for the background samples (concrete only). The dimensions of the concrete only background sample correspond to the size of the concrete object with an iron rod. Since the signal is defined as the sum of the absolute bin to bin differences, the signal for the no-rebar scenario is not 0. The signal increases monotonically with increasing rebar volume (blue dots). Hence, with this technique, it is possible to calculate the volume of rebars. However, the volume of the concrete, that is the background, also affects the signal value (black triangles). Thus, in the variable size concrete block scenario, the signal value depends on the iron volume and concrete volume as well. Nonetheless, with an independent way of measuring the size of the concrete structure, the only unknown variable will be the rebar volume.

To understand the potential of the technique better, a case with a growing rebar diameter in a fixed size concrete block (a description of this case is given in section 3.2) was studied. The signal value as a function of rebar volume is shown in figure 9. The signal follows a similar trend as for the variable sized concrete block, it increases monotonically with increasing rebar volume. Since it grows with a steep slope, it

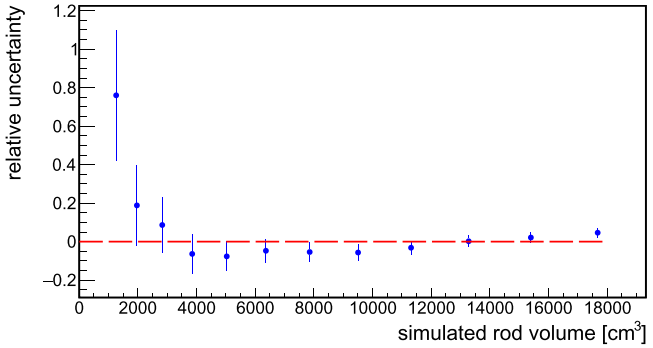

Figure 11. Relative uncertainty in the reconstructed volume as a function of the simulated rebar volume.

is possible to measure small volumes precisely, see section 5.2.

To determine the minimum volume of rebar that can be reliably detected, for the fixed sized concrete scenario, the simulation of the background case was repeated 14 times and the signal was calculated for each pair of simulated background samples. Next, the distribution of the background signal was prepared and from a Gaussian fit to this distribution, the mean, μ_b, and sigma, σ_b, were extracted and they are $3\ 994 \pm 44$ and 371 ± 34 respectively. The detection threshold for iron in concrete was set as $\mu_b + 3\sigma_b$ and it is equal to 5 107. In figure 9, it can be seen that this corresponds to a minimum volume that can be detected which is $894 \pm 386\,\text{cm}^3$. This threshold is marked in figure 9 as a

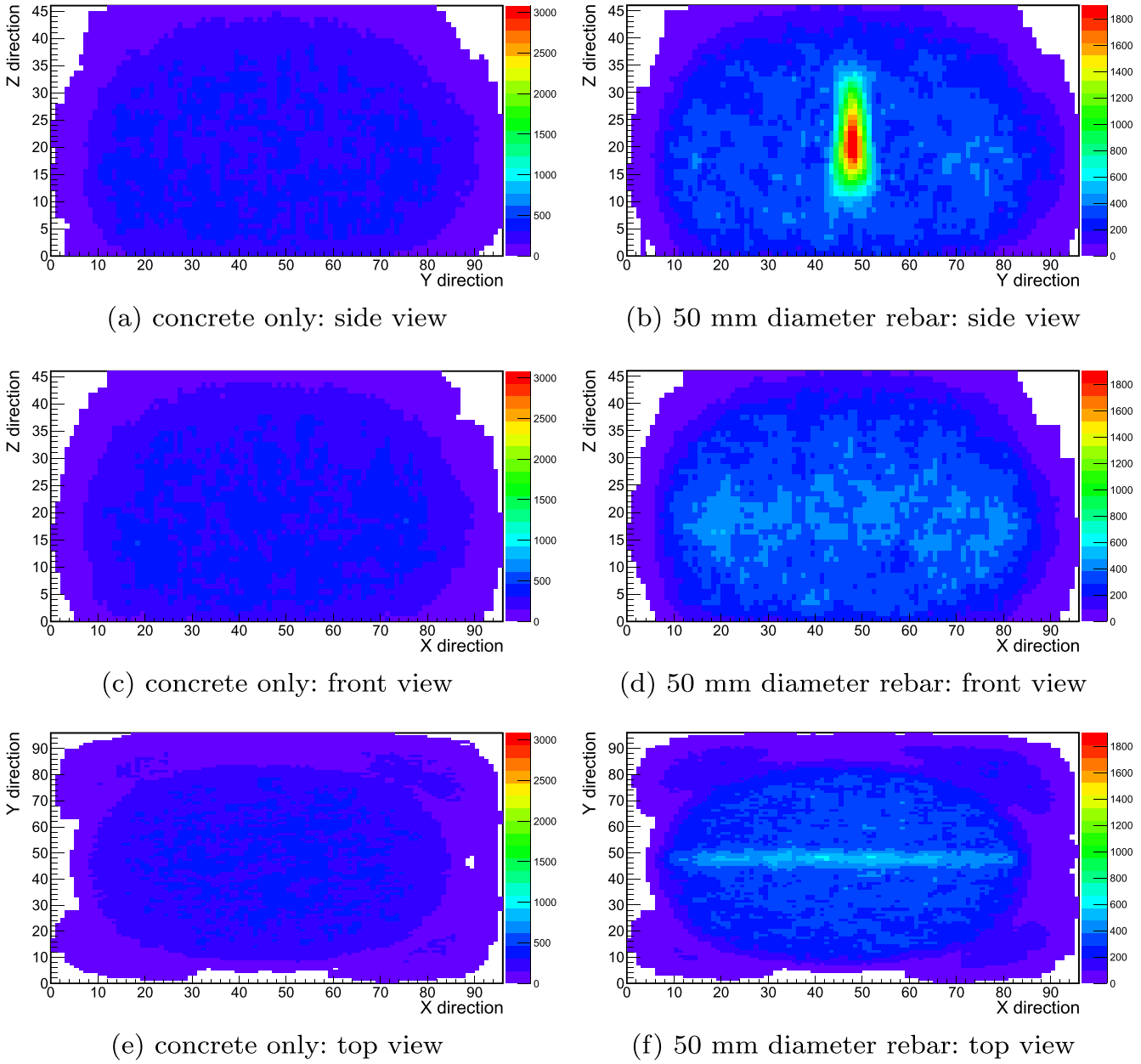

Figure 12. Images of an object of solid concrete structure contrasted with images of the concrete object with a 50 mm diameter rebar inside.

solid red line. This value corresponds to a diameter of 33.7 ± 7.3 mm for the 100 cm long rebars used in this study. The result demonstrates clearly that the presence of rebars of a realistic size can be detected reliably using MST.

5.2. Reconstruction of the rebar volume in the concrete object

The results presented in figure 9 show that the value of S varies rapidly with the rebar volume. Hence, S is a good way to measure the total volume of iron in a concrete sample. In this section, the resolution on the reconstructed rebar volume is presented. The results shown in figure 9 for the volume above the detection threshold were fitted with a linear fit. The resulting slope was 1.75 ± 0.03 and the offset $4\,997.3 \pm 333.0$. The χ^2/ndf was 13.37/10, showing that the data was well described by a linear dependence. The parameters of the linear fit were used to perform the reconstruction of the rebar volume. To reconstruct a volume, a linear dependence was fitted to all data points other than the one under study. Then, the rebar volume V_r for the volume under study was reconstructed by inverting the fitted formula. The reconstruction was performed for all simulated iron volumes above the detection threshold. Figure 10 shows the reconstructed volume as a function of the simulated volume. There is clear linear dependence between the reconstructed and actual volume (fit line slope was 0.997 ± 0.023, offset was 25.9 ± 213.2 and χ^2/ndf was 16.74/10). Figure 11 shows the relative uncertainty in the reconstructed volume as a function of the simulated rebar volume. Above 2 500 cm^3, which corresponds to a diameter of 56.4 mm for the 100 cm long iron rebars used in this study, the relative uncertainty is better than 10% and the volume of the rebar can be

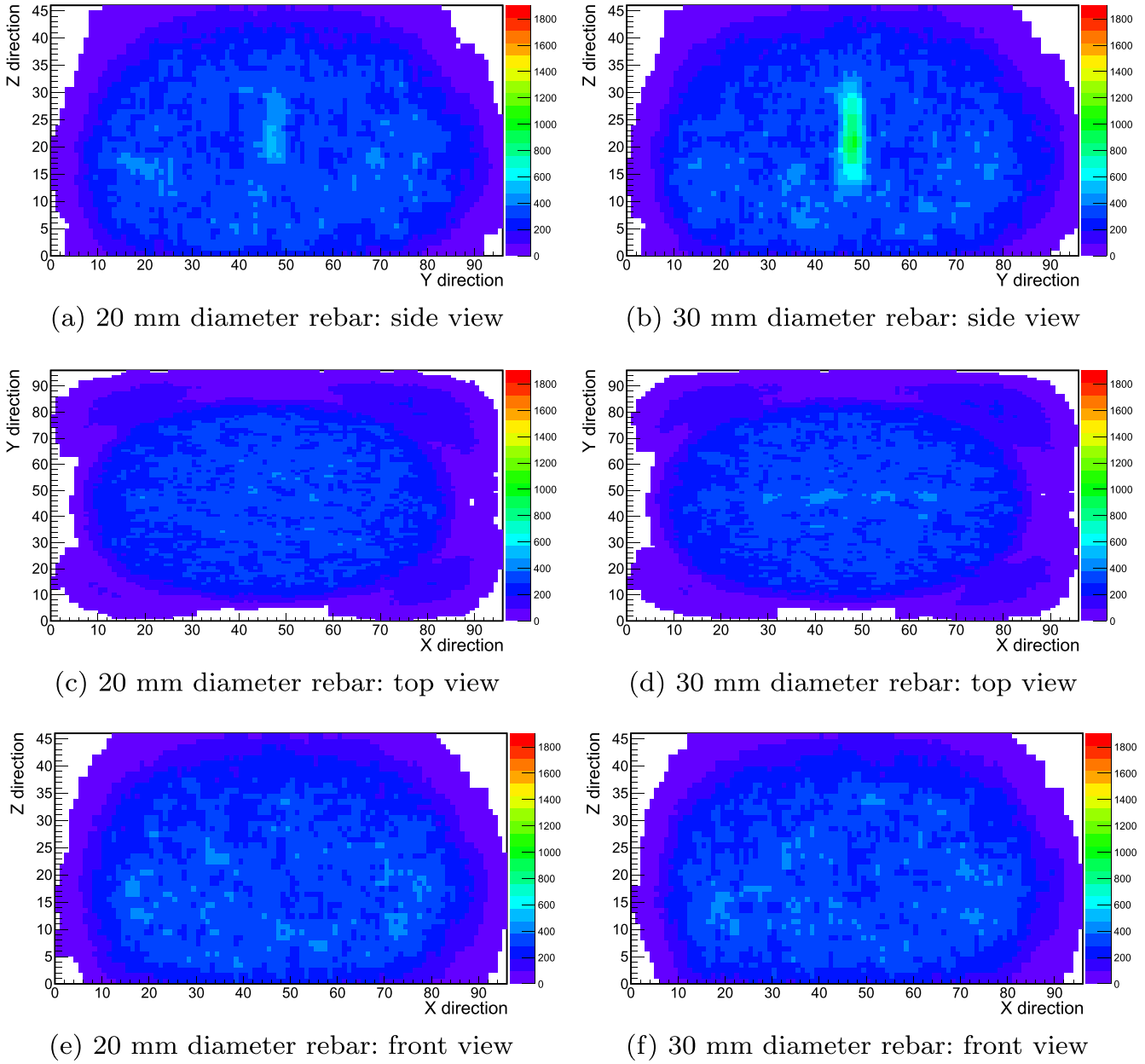

(a) 20 mm diameter rebar: side view

(b) 30 mm diameter rebar: side view

(c) 20 mm diameter rebar: top view

(d) 30 mm diameter rebar: top view

(e) 20 mm diameter rebar: front view

(f) 30 mm diameter rebar: front view

Figure 13. Images of the concrete object for the fixed size concrete blocks with rebars diameter of 20 (left) and 30 mm (right).

reconstructed with a resolution of 5.4% ± 0.3%. This shows that it is possible to achieve a good volume resolution on the rebars using this technique.

5.2.1. Summary of the detection and volume measurement. The results presented here demonstrate that it is possible to find iron inclusions inside concrete blocks and determine their volume using MST. The smallest volume of iron that could be detected is 894 ± 386 cm^3 which corresponds to a diameter of 33.7 ± 7.3 mm for the 100 cm long rebars used in this analysis. The relative uncertainty for the volumes above 2 500 cm^3, which corresponds to a diameter of 56.4 mm for the 100 cm long rebars used in this analysis, is below 10% and the rebar volume can be reconstructed with a resolution of 5.4% ± 0.3%, which is more than accurate enough for inspection of concrete structures. Although a diameter of 33 mm is quite large for rebars, the results do demonstrate that the technique works. Further work is ongoing to also detect thinner rebars.

6. Results: imaging of detected rebars

After an inclusion is detected in a scanned sample, the next step is to image it. Imaging complements the detection process. It answers the question of where the object is located and estimates its shape. The imaging of a detected object is done by applying the signal algorithm (details of the signal extraction are in section 4) to smaller sub-volumes of the scanned object. To get a complete image of the scanned object, this approach was applied to three projections

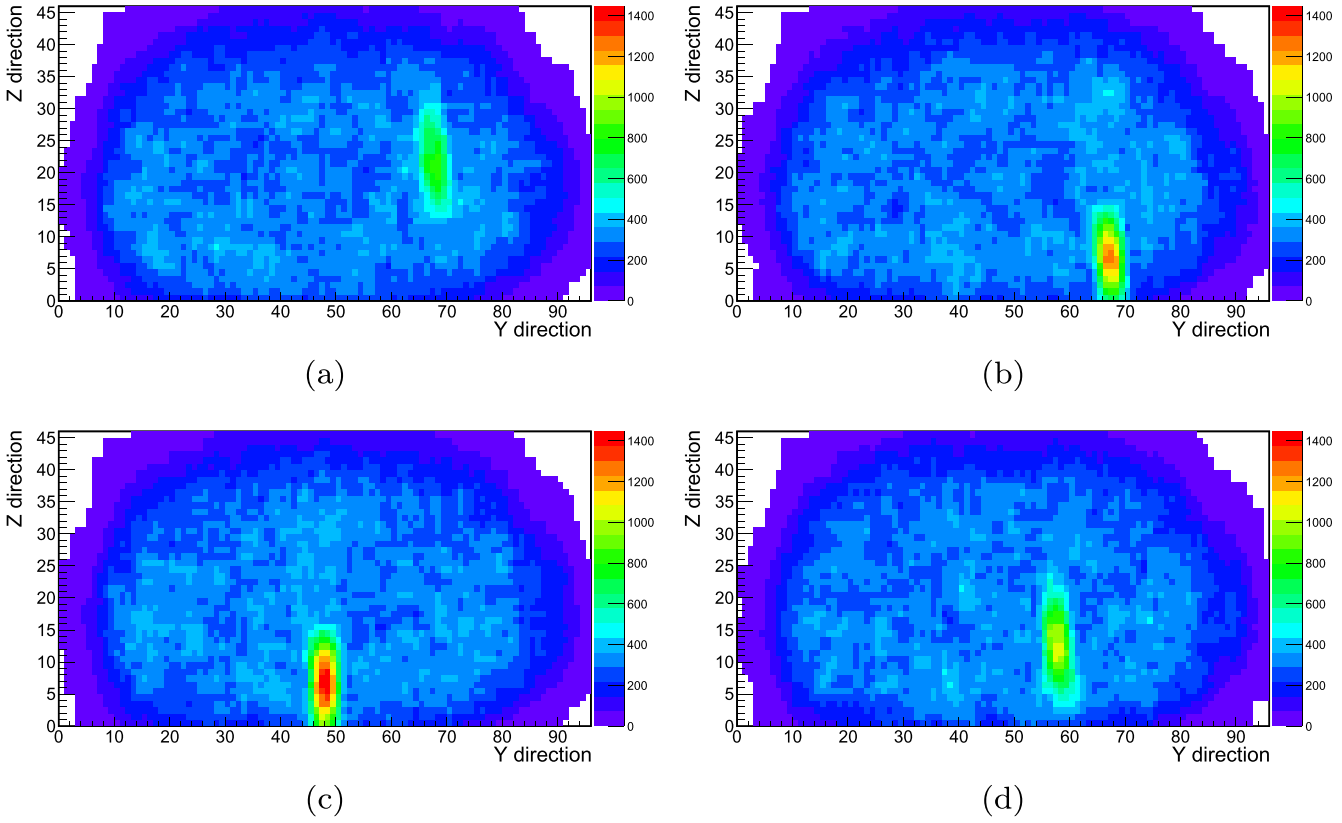

Figure 14. Rebar of 30 mm diameter placed in 4 different locations.

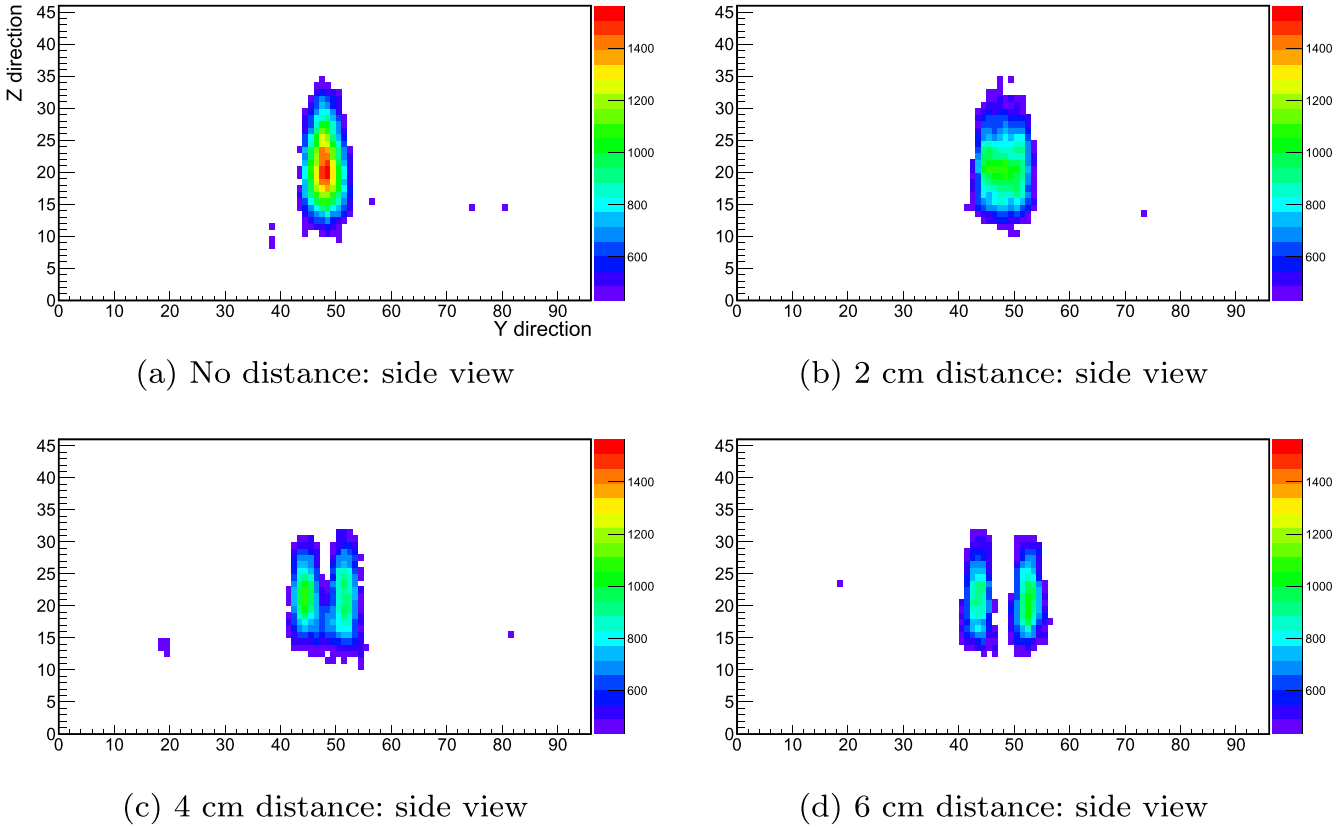

Figure 15. Two separated 30 mm diameter rebars after applying the threshold.

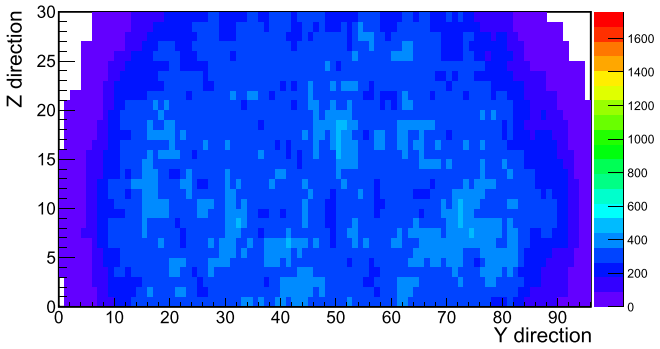

(a) concrete only: side view

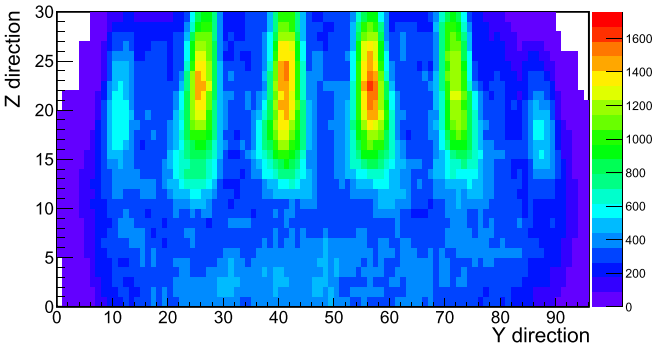

(b) rebars: side view

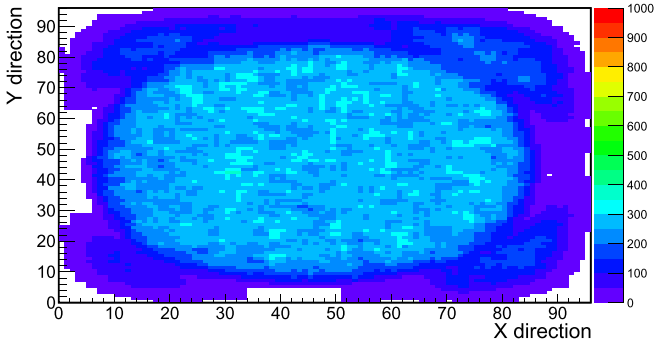

(c) concrete only: top view

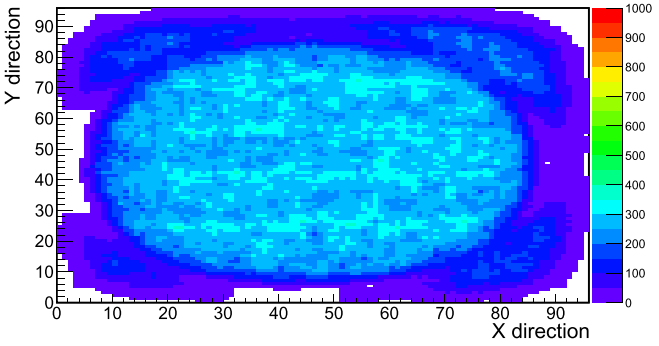

(d) rebars: top view

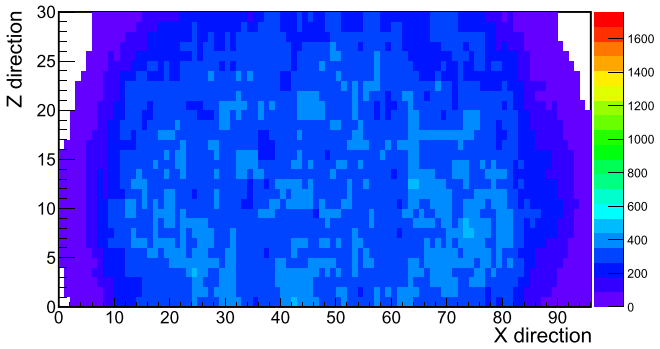

(e) concrete only: front view

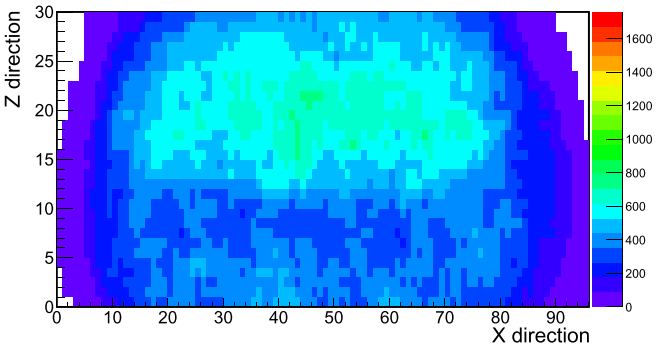

(f) rebars: front view

Figure 16. Results of the reinforcement imaging: concrete only and single layer of 30 mm diameter parallel rods.

separately: *ZY* (side view), *YX* (top view), *ZX* (front view). The steps to get the image are as follows:

1. The object under investigation is scanned for a certain time. Then, a concrete background sample with the same dimensions as the scanned object is simulated. The amount of simulated data must correspond to the amount of data taken during the scanning of the investigated object;
2. Next, a 3D sub-volume is defined using a sliding window. A 5 cm $\times$ 5 cm window in the *ZY* projection was chosen, integrating all discriminator values along *X* direction into one discriminator distribution;
3. When the discriminator distributions for sub-volumes for both background and object geometry are calculated, based on them, the signal for sub-volume is calculated;
4. The sub-volume is shifted and all the steps are repeated;
5. The grid is shifted until the whole object is scanned and the signal for each sub-volume is determined;
6. Finally, an image of the scanned object is prepared which is a two dimensional histogram of the signal from all sub-volumes;
7. The same steps are repeated for the remaining projections.

To explain the principle of the imaging process, images of no-rebar scenario and a scenario with 50 mm diameter rebar from the fixed size concrete block geometry are contrasted in figure 12. One bin of each histogram refers to one sub-volume and the color scale shows the signal of the sub-

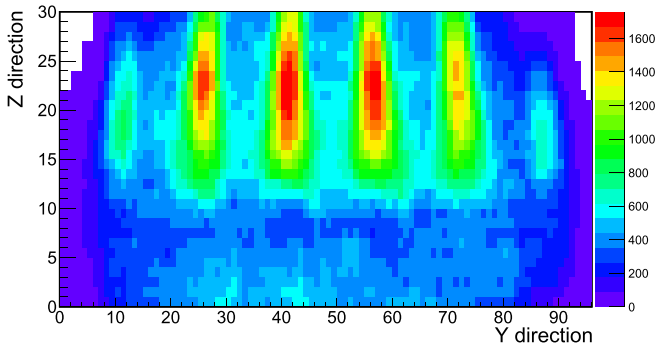

(a) single grid: side view

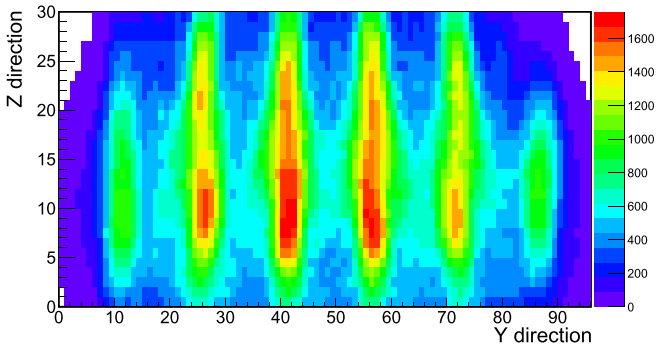

(b) double grid: side view

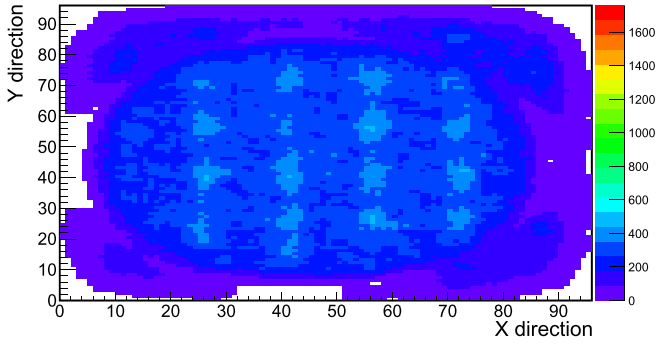

(c) single grid: top view

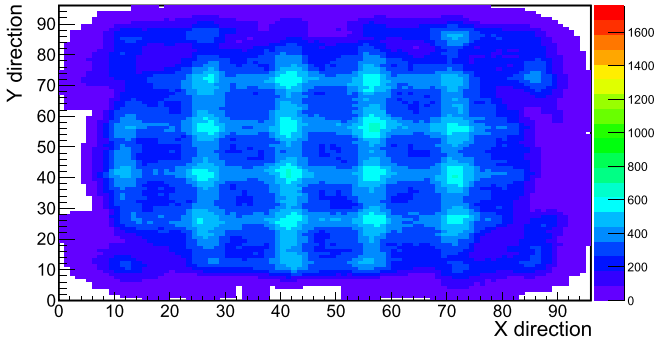

(d) double grid: top view

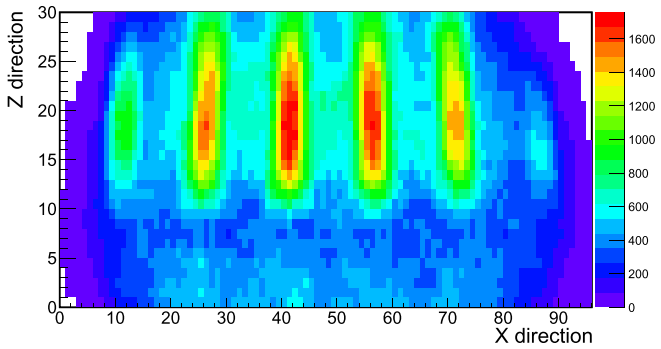

(e) single grid: front view

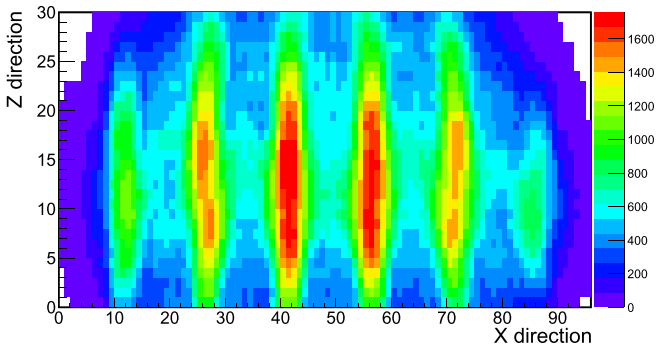

(f) double grid: front view

Figure 17. Results of the reinforcement imaging: single and double 30 mm diameter rebar grid.

volume. The range of the color axes of the histograms is kept the same to highlight the changes in the images with different content. There is a clear difference between the signal for the concrete only object (see figures 12(a), (c), (e)) and the signal obtained for the geometry with 50 mm diameter rebar in concrete (see figures 12(b), (d), (f)). The signal values of the scenario with rebar are much higher than signal calculated for the concrete-only object. The side view (*ZY* projection, figure 12(b)) clearly shows a roundish object placed in the center. The *YX* projection (top view, figure 12(f)) shows a long object in the center. The front projection (*ZX*) should show similar result as top view projection, but it shows a signal that is much higher than the signal obtained for the concrete only case but the histogram is blurred. The imaging including the *Z* views are smeared out due to well-known effect of *z*-blurring. Since most muons come in straight from the top (the *Z*-direction) and scatter with small angles, as a result there are large uncertainties of the scattering vertex position reconstruction along the *Z* axis. Therefore, the object in images along the *Z* axis is blurred. However, the vertices are very well constrained in the *X* and *Y* direction.

6.1. The images of concrete with rebar for the fixed size concrete block

More images of the concrete cuboids with rebars in the center for the fixed size concrete block are compared in figure 13 starting from the 20 mm diameter rebar. It is clearly seen that with increasing the size of the rebar diameter the signal becomes stronger. The imaging algorithm allows us to locate an object in concrete wall. It is also possible to evaluate the shape of the detected object.

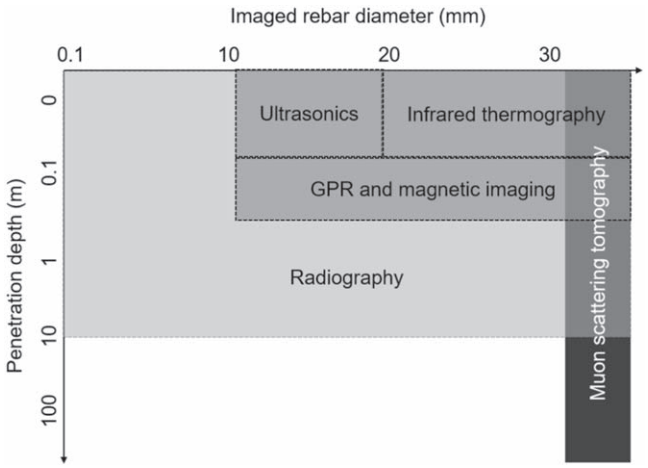

Figure 18. Rebar imaging capabilities of MST and other existing techniques in electromagnetic, thermal, ultrasonic and radiographic imaging [34–40, 42, 43].

In section 5.1 it was shown that with our algorithm, the smallest statistically reliably detectable rod is a rod with a diameter of 33.7 ± 7.3 mm for the 100 cm long rebars used in this study. In figure 13(b), a 30 mm diameter rod is clearly distinguishable by eye and in figure 13(a) hint of signal of 20 mm diameter rod is also visible.

A study was undertaken to show that the detection performance is independent of the location of the rebar. A 30 mm diameter rebar inside the block was simulated placed at four different locations. The results of this study are shown in figure 14. The rebar is still easy to detect, even if it is close to the edge of the concrete object. In all of the simulated cases the signal values are similar. Means of the signal distribution for the *ZY* projection are: for figure 14(a) is 221.3 ± 2.0 for figure 14(b) is 227.1 ± 2.3 for figure 14(c) is 231.0 ± 2.4 for figure 14(d) is 225.1 ± 2.1. Thus, the performance of the imaging algorithm is independent of the location of the rebar within the concrete sample. Hence, the location of the object can be determined with this algorithm.

6.2. Two separated rebars

In real structures, rebars can be close to each other, so the minimum distance between rebars where they can still be distinguished as separate objects was studied. In this study, concrete samples with two 30 mm diameter rebars were inserted in a fixed size concrete block and the distance between them was increased in steps of 2 cm starting from no distance. First, a simulation of the concrete only was performed (images shown in figures 12(a), (c), (e)) and a one-dimensional distribution of the side view projection of the signal values for the central region created. This distribution was fitted with a Gaussian. The fit result was used to determine a minimum signal threshold for the presence of rebars. Two separate objects were stated to be detected if five or more bins in the area between the two objects show a signal below this threshold. Here the Gaussian fit yielded a mean of 295 ± 1 and a sigma of 46 ± 1. The threshold was set a $\mu_s + 3\ \sigma_s = 433$. Figure 15 shows the results after applying the threshold. The image shows that separations between two bars starts to be observed if the spacing is at least 4 cm. The bars are observed as fully separate objects when the spacing is 6 cm or more.

7. Results: imaging of rebar cages

The results presented above clearly demonstrate that single rebars encased in concrete can be detected and imaged using MST. Here, results of the imaging of reinforced concrete as detailed in section 3.3 and illustrated in figure 7, are presented. First of all, a background sample was imaged and the mean of the signal distribution is 256.5 ± 2.1, 163.1 ± 1.1, 255.4 ± 2.2, accordingly for projections in figures 16(a), (c), (e). Next, the concrete object with one layer of parallel rebars was imaged, see figures 16(b), (d), (f). In the *ZY* projection (figure 16(b)) all simulated bars are visible, but they are smeared out due to the z-blurring effect. In the *YX* projection (figure 16(d)) four of the rebars are distinguishable by eye. The outer two rebars are not visible because of the limited acceptance of the simulated 1 × 1 m^2 detector system. In the *ZX* plane (rebar axial plane, figure 16(f)) rebars can also been seen, albeit not so clear due to the *z*-blurring.

A grid of rebars inside the concrete was imaged. The results are shown in figures 17(a), (c), (e). In comparison to the image of the parallel rebars only, the signal values are much stronger, reflecting the additional amount of iron. In the top view projection, see figure 17(c), the simulated grid is visible. Finally, the results for the two layers of grid are shown in figures 17(b), (d), (f). In all projections, the signal of the double-layer of the grid is much stronger than the signal from the single grid layer. The signal strength allows to differentiate between the presence of a single or a double layer of grid. Due to the *z*-blurring the two layers merge into one in the *ZX* and *ZY* projections. However, the length in *Z* of the signal extends over much larger values of *Z*, which also allows to differentiate between a single and a double layer of grid being present. Hence, the algorithm does also work for more complicated and realistic scenarios and does show promise for practical and industrial applications.

7.1. Critical comparison with existing imaging methods

The imaging performance of existing rebar detection methods [30–33] is compared with the current state of MST in figure 18. At the time of writing, the most commonly used techniques in practice are magnetic imaging and ground penetrating radar (GPR) [34–36]. These techniques can image 10–20 mm diameter rebars at depths of 100–500 mm. Meanwhile, imaging based on infrared thermographics [37, 38] and ultrasonics [39, 40] can fill any need for low-depth imaging at <20 cm. All of these techniques excel in quantifying element thickness and rebar location, but precise rebar size estimation is still an ongoing challenge [35]. Errors dramatically increasing with penetration depth and rebar congestion [41], and accurate imaging beyond the first or second rebar layer is often impossible. High resolution and

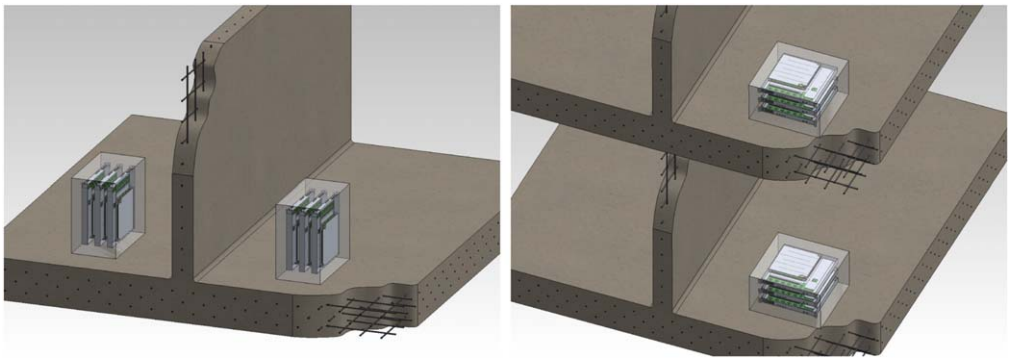

Figure 19. Sketches indicating how a wall (left) and floor (right) scan would be undertaken.

high depth imaging can, at least from a technical standpoint, be realized using x-ray and neutron radiography [42, 43]. However, as the use of active sources of radiation presents an acute risk to human health, it is rare to see these techniques applied outside of laboratory post-mortem testing.

There is therefore still an unmet need for high depth, high resolution imaging that MST could bridge with further development. In this work, we have reported a lower imaging resolution for MST that is subject to z-blurring, but this should be taken in light of the fact that the technology has only just started to be developed for rebar imaging: the other techniques in figure 18 have already enjoyed 30–50 years of development, and have inherent limitations on imaging depth. What is more, MST is not affected (unlike GPR) by the ground moist or fine silts. Further development of MST to improve resolution could therefore unlock a new imaging technique which fulfills the need for a safe imaging method which can scan beyond the first rebar layer.

8. Deployment

The method detailed in this paper is capable of detecting rebars in floors and walls. So far this has only been shown in realistic simulations using the measured performance of our prototype detectors and validated muon flux simulations. Currently, we are building a system based on the detectors described in section 2.3 and shown in figure 5 to start field trials. In such trails two stacks of detectors are placed either side of the wall or floor, as shown in figure 19. Ideally, the detectors are placed as close as possible to the object to be scanned and each other. This is because for the scan, the muon needs to traverse both detector stacks. By placing them as close as possible together, the acceptance is maximized. When scanning floors, this is not always possible. However, as the scattering in air is negligible, one stack can be placed on the floor below. Although this reduces the acceptance and increases the extrapolation error for the muon track through the bottom stack, good scan results can still be obtained.

9. Conclusions

There is a need in civil engineering for NDE techniques to image the internal structures of concrete to inform decisions around structural maintenance and modification. Monte Carlo simulations were used to show that MST is an effective technique to image rebars within thick concrete objects. Different geometries were simulated to reproduce realistic scenarios for rebar configurations within concrete structures. Using the metric method, rebars with a diameter as small as 33.7 ± 7.3 mm with a length of 100 cm are detected. Currenhtttly, more study is being done to adjust the method in detecting smaller rods. It was shown that the signal value has monotonic dependence on the volume of the content of concrete, which allows to measure the volume of the inclusion with a resolution of $5.4\% \pm 0.3\%$, and relative uncertainty below 10%, for rebar volumes above 2 500 cm^3. Moreover, the result is independent of the location of the rebar. Rebars placed as close as 6 cm apart can be distinguished as two separate objects, however the separation starts to be visible with the spacing of 4 cm. The technique also allows for the imaging of rebar structures in reinforced concrete and differentiation between single and double layers of rebar grids with rod diameters of 30 mm. This demonstrates that the technique is a viable option for practical trials in future work.

ORCID iDs

Magdalena Dobrowolska https://orcid.org/0000-0002-9851-8814

References

[1] Get it Right Initiative Ltd. https://getitright.uk.com/live/files/reports/3-giri-research-report-revision-3-284.pdf (accessed:10 September 2019)

[2] Hanke R, Fuchs T and Uhlmann N 2008 X-ray based methods for non-destructive testing and material characterization *Nuclear Instruments and Methods in Physics Research Section A: Accelerators, Spectrometers, Detectors and Associated Equipment* **591** (1) 14-18

[3] International Atomic Energy Agency 1996 Manual on Gamma Radiography, Practical Radiation Safety Manual No. 1, IAEA, Vienna ().International https://www.iaea.org/publications/4571/manual-on-gamma-radiography

[4] International Atomic Energy Agency 2008 *Neutron Imaging, A Non-Destructive Tool for Materials Testing* IAEA-TECDOC-1604, Report of a coordinated research project https://www-pub.iaea.org/MTCD/publications/PDF/te_1604_web.pdf

[5] Alvarez L W *et al* 1970 Search for hidden chambers in the pyramids *Science* **167** 832–9

[6] Nagamine K, Iwasaki M, Shimomura K and Ishida K 1995 Method of probing inner-structure of geophysical substance with the horizontal cosmic-ray muons and possible application to volcanic eruption prediction *Nucl. Instrum. Methods Phys. Res.* A **356** 585–95

[7] Miyadera H, Borozdin K N, Greene S J, Lukić Z, Masuda K, Milner E C, Morris C L and Perry J O 2013 Imaging fukushima daiichi reactors with muons *AIP Adv.* **3** 052133

[8] Borozdin K, Greene S, Lukić Z, Milner E, Miyadera H, Morris C and Perry J 2012 Cosmic ray radiography of the damaged cores of the fukushima reactors *Phys. Rev. Lett.* **109** 152501

[9] Thomay C, Velthuis J J, Baesso P, Cussans D, Morris P A W, Steer C, Burns J, Quillin S and Stapleton M 2013 A binned clustering algorithm to detect high-z material using cosmic muons *J. Instrum.* **8** P10013

[10] Thomay C, Velthuis J J, Baesso P, Cussans D, Steer C, Burns J, Quillin S and Stapleton M 2015 A novel Markov random field-based clustering algorithm to detect high-z objects with cosmic rays *IEEE Trans. Nucl. Sci.* **62** 1837–48

[11] Thomay C, Velthuis J, Poffley T, Baesso P, Cussans D and Frazão L 2016 Passive 3d imaging of nuclear waste containers with muon scattering tomography *J. Instrum.* **11** P03008

[12] Frazão L, Velthuis J, Thomay C and Steer C 2016 Discrimination of high-z materials in concrete-filled containers using muon scattering tomography *J. Instrum.* **11** P07020

[13] Dobrowolska M, Velthuis J, Frazão L and Kikoła D 2018 A novel technique for finding gas bubbles in the nuclear waste containers using muon scattering tomography *J. Instrum.* **13** P05015

[14] Frazão L, Velthuis J J, Maddrell-Mander S and Thomay C 2019 High-resolution imaging of nuclear waste containers with muon scattering tomography *J. Instrum.* **14** P08005

[15] Clarkson A *et al* 2015 Characterising encapsulated nuclear waste using cosmic-ray muon tomography **10** P03020 arXiv:1410.7192

[16] Tanaka H K M, Nagamine K, Nakamura S N and Ishida K 2005 Radiographic measurements of the internal structure of mt. west iwate with near-horizontal cosmic-ray muons and future developments *Nucl. Instrum. Methods Phys. Res.* A **555** 164–72

[17] Ambrosi G *et al* 2011 The mu-ray project: Volcano radiography with cosmic-ray muons *Nucl. Instrum. Methods Phys. Res.* A **628** 120–3

[18] Carloganu C *et al* 2013 Towards a muon radiography of the puy de dôme *Geosci. Instrum. Methods Data Syst.* **2** 55–60

[19] Borozdin K N, Hogan G E, Morris C, Priedhorsky W C, Saunders A, Schultz L J and Teasdale M E 2003 Surveillance: radiographic imaging with cosmic-ray muons *Nature* **422** 277

[20] Baesso P, Cussans D, Thomay C and Velthuis J 2014 Toward a rpc-based muon tomography system for cargo containers *J. Instrum.* **9** C10041

[21] Beringer J *et al* (Particle Data Group collaboration) 2012 Review of particle physics *Phys. Rev.* D **86** 010001

[22] Reyna D 2006 A simple parameterization of the cosmic-ray muon momentum spectra at the surface as a function of zenith angle arXiv:hep-ph/0604145

[23] Eidelman S *et al* 2004 Review of particle phy+sics *Phys. Lett.* B **592**

[24] Schultz L J 2003 Cosmic ray muon radiography *PhD Thesis* Portland State University Portland, OR, USA http://citeseerx.ist.psu.edu/viewdoc/download?doi=10.1.1.308.810&rep=rep1&type=pdf

[25] Schultz L J, Blanpied G S, Borozdin K N, Fraser A M, Hengartner N W, Klimenko A V, Morris C L, Orum C and Sossong M J 2007 Statistical reconstruction for cosmic ray muon tomography *IEEE Trans. Image Process.* **16** 1985–93

[26] Stapleton M, Burns J, Quillin S and Steer C 2014 Angle statistics reconstruction: a robust reconstruction algorithm for muon scattering tomography *J. Instrum.* **9** P11019

[27] Baesso P, Cussans D, Thomay C, Velthuis J J, Burns J, Steer C and Quillin S 2013 A high resolution resistive plate chamber tracking system developed for cosmic ray muon tomography *J. Instrum.* **8** P08006

[28] Hagmann C, Lange D and Wright D 2007 Cosmic ray shower generator (cry) for monte carlo transport codes *Nuclear Science Symp. Conf. Record, 2007. NSS'07. IEEE* vol 2 (Piscataway, NJ: IEEE) pp 1143–6

[29] Agostinelli S *et al* 2003 Geant4 a simulation toolkit *Nucl. Instrum. Methods Phys. Res.* A **506** 250–303

[30] Verma S K, Bhadauria S S and Akhtar S 2013 Review of nondestructive testing methods for condition monitoring of concrete structures *J. Constr. Eng.* **2013** 1–11

[31] Dérobert X, Aubagnac C and Abraham O 2002 Comparison of NDT techniques on a post-tensioned beam before its autopsy *NDT&E Int.* **35** 541–8

[32] Büyüköztürk O 1998 Imaging of concrete structures *NDT&E Int.* **31** 233–43

[33] Pla-Rucki G F and Eberhard M O 1995 Imaging of reinforced concrete: state-of-the-art review *J. Infrastruct. Syst.* **1** 134–41

[34] Bungey J H 2004 Sub-surface radar testing of concrete: a review *Constr. Build. Mater.* **18** 1–8

[35] Tarussov A, Vandry M and De La Haza A 2013 Condition assessment of concrete structures using a new analysis method: ground-penetrating radar computer-assisted visual interpretation *Constr. Build. Mater.* **38** 1246–54

[36] Rathod H, Debeck S, Gupta R and Chow B 2019 Applicability of GPR and a rebar detector to obtain rebar information of existing concrete structures *Case Stud. Constr. Mater.* **11** e00240

[37] Milovanović B and Pečur I B 2016 Review of active IR thermography for detection and characterization of defects in reinforced concrete *J. Imaging* **2** 11

[38] Maierhofer C, Arndt R and Röllig M 2007 Influence of concrete properties on the detection of voids with impulse-thermography *Infrared Phys. Technol.* **49** 213–7

[39] Burrascano P, Callegari S, Montisci A, Ricci M and Versaci M 2014 *Ultrasonic Nondestructive Evaluation Systems: Industrial Application Issues* (Berlin: Springer) ISBN: 978-3-319-10566-6

[40] Laureti S, Ricci M, Mohamed M N I B, Senni L, Davis L A J and Hutchins D A 2018 Detection of rebars in concrete using advanced ultrasonic pulse compression techniques *Ultrasonics* **85** 31–8

[41] Chang C W, Lin C H and Lien H S 2009 Measurement radius of reinforcing steel bar in concrete using digital image GPR *Constr. Build. Mater.* **23** 1057–63

[42] du Plessis A and Boshoff W P 2019 A review of x-ray computed tomography of concrete and asphalt construction materials *Constr. Build. Mater.* **199** 637–51

[43] Zhang P, Wittmann F H, Lura P, Müller H S, Han S and Zhao T 2018 Application of neutron imaging to investigate

fundamental aspects of durability of cement-based materials: a review *Cem. Concr. Res.* **108** 152–66